Density Functional Theory Studies of Doping in Titania

Run Long and Niall J. English[a)]

The SEC Strategic Research Cluster and the Centre for Synthesis and Chemical Biology, Conway Institute of Biomolecular and Biomedical Research, School of Chemical and Bioprocess Engineering, University College Dublin, Belfield, Dublin 4, Ireland

The structural and electronic properties of rutile and anatase, and the influence of both mono- and co-doping, have been studied using Density Functional Theory. Ge-doped anatase and rutile exhibit different band gap-narrowing mechanisms; in particular, host Ti 3d states move to lower energy regions in anatase and Ge 4s impurities states locate below the conduction band of rutile. For S-doping, S 3p states locate above the top of the valence band and mix with O 2p states, leading to band gap narrowing. For Bi-doping, the energy levels of the Bi 6s states lie below the bottom of the conduction band while the Fermi level E_F lies above the gap states, indicating the gap states are fully occupied. For Bi/S–codoping, both S 3p acceptor states and partially occupied Bi 6s donor states hybridised with S 3p appear simultaneously. For N- and W-monodoping, isolated N 2p states above the top of the valence band and W 5d states below the conduction band lead to band gap narrowing. N/W codoping yields significant band gap narrowing. Both studies for Bi/S and N/W

[a)] Corresponding author. Electronic Mail: niall.english@ucd.ie

codoping rationalise recent experimental data which show that these doped anatase systems exhibit higher visible-light photocatalytic efficiency than respective monodoping.

Keywords: Ge-doped, Bi/S-doped, N/W-doped, electronic structure, TiO_2

Introduction

Titania (TiO_2) has received intense attention as a promising photocatalytic material for many years [1, 2]. The large band gap of TiO_2 (3.2 eV for anatase [3] and 3.06 eV for rutile [4]) restricts its photocatalytic application to the ultraviolet range, and thus only about 3-5% of total sunlight can photo-activate this metal oxide to promote reduction and oxidation surface processes [2]; further, photoexcited electron-hole pairs may recombine relatively easily, restricting photocatalytic activity. The shift of titania's optical absorption edge to the visible-light region has become one of the most important subjects in photocatalyst applications. Many approaches have been attempted, such as doping of various transition metal cations [5-7] and synthesis of reduced TiO_{2-x} (e.g., formation of oxygen vacancies) [8, 9]. The use of quantum simulation methods, such as density functional theory (DFT), as a design tool to predict the electronic structure of potential photocatalytic materials and to 'filter' the most promising ones prior to experimental work is clearly attractive. However, the accurate characterization of the electronic structure of titania by means of density functional theory (DFT) remains elusive, although there have been a number of studies devoted to this [10]. The band gaps of transition metal oxides are usually underestimated by DFT because of the less accurate description of the strong Coulomb and exchange interactions between electrons in the same *d*-shell.

The aim of this study is to compare and contrast generalized gradient approximation (GGA) approaches to the prediction of electronic structure in anatase and rutile. We have used the Perdew-Burke-Ernzerhof (PBE) and Perdew-Wang

functionals with norm-conserving local and projector augmented wavevector (PAW) pseudopotentials, respectively. We also used the GGA+U approach introduced by Dudarev et al. [11] to set the *d*-shell electronic interactions as strongly correlated states while leaving the other orbitals delocalized, in an effort to improve the treatment of electronic properties by DFT. and considered to be described properly by the GGA approach.

This article also seeks to use DFT to explore how mono- and co-doping may be used to extend titania's optical absorption edge to the visible-light region, and to rationalise simulation results with available experimental observations, where possible. Doping with metals and nonmetals [12-20] has been used widely. However, reported studies of codoping with both metal and nonmetal elements are significantly more rare. Recently, Asahi et al. [17] reported that N-doped TiO_2 shows a significant improvement over pure TiO_2 in its optical absorption and photocatalytic activity for visible light. Subsequent studies reported several other visible light-activated S- [19, 21, 22] and B-doped TiO_2 cases [20, 23]. C-doped TiO_2 has been the subject of significant scrutiny since Sakthivel et al. [24] reported that C-doped TiO_2 powder is roughly five times more active than N-doped titania in the degradation of 4-chlorophenol by artificial light ($\lambda \geq 455$ nm). Other experiments have been carried out by other groups which reported the red-shift of the optical absorption edge [25, 26]. However, the nature of C-induced modifications to the TiO_2 electronic band structure is controversial. Both band gap narrowing [27] and the formation of localized mid-gap states [28] have been proposed for the red-shift of the optical

absorption edge. In addition, Sn-doped TiO_2 has also attracted much attention, with Sn-doped rutile TiO_2 reported to lead to a red-shift of the optical absorption edge [29], while other results indicate blue-shifting in Sn-doped anatase [30]; these experimental observations have been confirmed by our previous theoretical studies [31]. Following this, we presented systemic geometrical and electronic properties comparison as well as photocatalytic activity of group-IV (Si, Ge, Sn, Pb) doped-TiO_2 using GGA method [32]. The results can explain well the Chatterjee et al. [33] experimental data of Ge impurites inducing a reduction in the band gap of Ge-doped anatase TiO_2. In the present study, we have further performed calculations of the geometrical and electronic structure properties for substitutionally Ge-doped rutile to compare the GGA +u and GGA results in detail. Our theoretical analysis provides a possible explanation for the experimentally observed band gap reductions in Ge-doped TiO_2 [33]; it is speculated that Ge-doped TiO_2 may be used for water splitting under visible light irradiation both from GGA and GGA+U, consistent with our previous work [32].

Given the relative paucity of experimental or theoretical studies of non-metal/metal codoping in titania, the study of Gai et al. [34] offers the possibility of modulating the band edges of TiO_2 to match visible light absorption through codoping by suitable nonmetal and metal elements. With this in mind, we have extended the present study to study Bi/S and N/W codoping. To date, there are few studies concerned with Bi/S-doped TiO_2 used as visible light-activated photocatalysts, besides Wang et al. [35], which reported that anatase co-doping with Bi and S can improve photocatalytic activity significantly and extend the absorption edge to 500-800 nm. They ascribed

the highly active photocatalytic performance to arise from the existence of numerous oxygen vacancies, the acidic sites on the surface of TiO_2, and the high specific surface area. Our theoretical analysis provides a possible explanation for the experimentally observed red-shift of the optical absorption edge and higher photocatalytic activity of Bi/S-doped TiO_2 [36]; we also discuss the thermodynamic properties of S-, Bi-, and Bi/S-doped anatase based on estimates of the formation energies.

N-doped TiO_2 is considered to be one of the most effective photocatalysts and it has been investigated widely, both by experimental and theoretical methods [17]. However, the nature of N-induced modifications to the electronic band structure depends on the doping content. Either band gap narrowing [17] or formation of localized midgap states [18] have been proposed for red-shifts of the optical absorption edge. Asahi et al. [17] concluded from first-principles calculations that N atoms were substituted for lattice O atoms causing narrowing of the band gap by mixing of N 2p and O 2p states. Conversely, Irie et al. [18] have suggested that the visible-light response in N-doped TiO_2 may be due to N 2p states isolated above the valence band maximum. In principle, WO_3 coupling has been used widely to improve the photocatalytic performance of TiO_2, because it reduces the recombination of electron-hole pairs [37] and expands the range of useful excitation radiation to the visible region. Recently, many experiments have focused on the addition of W to N-doped TiO_2 to increase photocatalytic activity under visible light irradiation [38, 39]. We have used GGA calculations to rationalise the origin of experimentally observed red-shifts in the optical absorption edge and synergetic effects of

N/W-codoping in anatase [40]. We also discuss the thermodynamic properties of N-, W-, and N/W -doped TiO_2 from analysis of calculated formation energies.

Methodology

The PBE [41] treatment of the exchange-correlation potential has been shown to be appropriate for titania [42]. For simulation of pure titania, 2x2x3 rutile and 2x2x1 anatase supercells were constructed according to the experimental geometry, containing 72 and 48 atoms, respectively. Local norm-conserving pseudopotentials for O and Ti were constructed with energy cut-offs of 80 Rydberg using the fhi98PP program [43]. The CPMD software package [44] was then used to optimize the wavefunction and geometry of the system to relative gradients of less than 10^{-5} and 10^{-4}, respectively, using an 80 Ryd energy cut-off. The Lanczos diagonalization was then carried out on the optimised system with sufficient number of Kohn-Sham orbital states in Krylov subspace to determine the orbital occupancy and eigenvalues, and the band gap determined from the HOMO-LUMO gap: since rutile has a direct band gap, Γ point sampling is sufficient.

Using pure titania as a reference, we wished to assess the effect of an alternative exchange-correlation functional and an all-electron pseudopotential. For the Perdew-Wang exchange-correlation [45], the calculations were performed using the all-electron PAW pseudopotentials, as implemented in the Vienna Ab Initio Simulation Program (VASP) code, version 4.6 [46, 47]. For the pure titania calculations, 48-atom (2×2×1) anatase and (2×2×2) rutile supercells were used. The

electronic wavefunction was expanded in plane waves up to a cutoff energy of 400 eV and a Monkhorst–Pack *k*-point mesh [48] of 4×4×4 was used for geometry optimization and electronic property calculations, using the block Davidson scheme [49, 50] for geometry optimization. Both atomic positions and cell parameters were optimized until the residual forces were below 0.01 eV/Å.

In the GGA+U treatment, a set of atomic-like orbitals is treated with a new Hamiltonian [51], which depends on the difference term U = U' – J, where U' describes the energy increase for an extra electron on a particular site, and J represents the screened exchange energy. For the pure titania calculations, we used the on-site Coulomb interaction parameter, U, of 5.8 eV for Ti 3d electrons [51]. This value is in good agreement with those reported for titania from x-ray photoemission spectroscopy experiments (XPS) and electron energy loss spectroscopy (EELS) ranging from 4 to 5 eV [52-55]. In addition, recent theoretical studies have also shown that a U term of approximately 5.5 ± 0.5 eV is most appropriate [56]. Further, Yang et al. have shown that this GGA + U method and U value is sufficient to describe the electronic structures of titania with the same 48-atom supercell [57]. The GGA+U calculations were performed in the same manner as the Perdew-Wang case.

Following validation of the PAW pseudopotential approach for pure titania, calculations for Ge, Bi/S and N/W (co-)doping were performed with this methodology as implemented in VASP, version 4.6, using the Perdew-Wang exchange-correlation potential for Ge and N/W and the PBE treatment for Bi/S. In these cases, the same plane-wave cut-off for the electron wave function, Monkhorst–Pack *k*-point mesh and

residual force termination gradient for geometry optimisation as above were employed. For Ge-doping, we used the same on-site Coulomb interaction parameter of U = 5.8 eV for Ti 3d electrons.

Ge-doped TiO_2 was modelled by single substitution of one Ge atom for one Ti atom (Ge@Ti) in 48-atom (2 × 2 × 1) anatase and (2 × 2 × 2) rutile supercells, whose structures are shown in Figures 1 and 2, respectively. For Bi/S doping, the S atom was substituted for an O atom (S@O) and the Bi atom for a Ti atom (Bi@Ti) in the 2 × 2 × 1 anatase system, while Bi/S-codoping was modelled by a single substitution of S for one O atom, and of one adjacent (nearest-neighbor) Ti atom replacement by substitution of a Bi atom. The free energy of this optimized configuration was evaluated to be some 0.3 eV lower than the next lowest free-energy optimised configuration, in which the Bi and S dopant atoms were as far apart as possible (one dopant in the center of the supercell with the other in a corner); a variety of different co-doping placement strategies were attempted. The atomic concentration of impurity was 2.08 %, which was comparable to that used experimentally [35]. To verify the effects of different doping levels of S and Bi on electronic structure, further calculations were carried out for anatase systems using a 96-atom supercell. The electronic structures of S-, Bi-, and Bi/S-doped TiO_2 at this doping concentration (half of that in the 48-atom case) showed nearly the same behavior as those found for the 48-atom supercell calculations [36], suggesting that our results are valid for the 48-atom supercell, in which interactions between dopants are negligible.

[insert Figs. 1 & 2 about here]

For N/W doping, the N atom was substituted for an O atom (N@O) and the W atom for a Ti atom (W@Ti) in the 2 × 2 × 1 anatase system, while N/W-codoping was modelled by a single substitution of N for one O atom, and of one adjacent (nearest-neighbor) Ti atom replacement by substitution of a W atom. Here, calculations show that the formation of an adjacent pair of N and W is energetically favourable by 0.57 eV vis-à-vis other N-W configurations [40]; this finding is supported by Raman and X-ray diffraction (XRD) measurements [39].

Results and Discussions

Pure titania

The optimised unit cell parameters are summarized in Tables 1 and 2 for anatase and rutile, respectively, for the Perdew-Wang GGA and GGA+U methods. These were a = 3.800 Å and c = 9.483 Å for pure anatase with the GGA method and a = 3.888 Å and c = 9.522 Å with GGA+U technique. Although both methods overestimate the lattice parameters with respect to the experimental value of a = 3.782 Å and c = 9.502 Å [58], the GGA results are better than those of the GGA+U method due to the parameter U increasing the interatomic interaction between *d* electrons. The GGA and the GGA + U calculations both overestimate the cell parameters of pure rutile (cf. Table 2). However, similar to the results of anatase, the GGA calculations are in closer agreement with the experimental values than the GGA + U case.

[insert Tables 1 & 2 about here]

In the PBE case, the direct band gaps (Γ to Γ) of the optimized rutile and anatase systems were determined to be 2.43 and 2.64 eV, respectively. For Perdew-Wang, the corresponding respective band gap results were approximately 1.7 and 2.0 eV employing the GGA method, respectively, which are in agreement with previous theoretical studies [57]. However, these values underestimate significantly the experimental values (3.2 eV for anatase and 3.0 eV for rutile). The Perdew-Wang GGA+U results were 2.84 and 2.38 eV for anatase and rutile, respectively, which is in better agreement with experimental values than the GGA technique. The calculated densities of states (DOS) of anatase and rutile are shown in Figures 3 and 4, respectively (left panel for GGA calculations and right panel for the GGA + U case). The valence band is composed mostly of O 2p states and the conduction band is dominated by Ti 3d states.

[insert Figs. 3 & 4 about here]

Ge Doping

We investigate firstly the effects of Ge-doping on the structure of anatase. The optimised unit cell parameters are summarised in Table 3. For the Ge-doped anatase (Ge@Ti) system, the crystal structure remained tetragonal while the cell parameters *a*

(*b*) and *c* are smaller and larger than the corresponding parameters of pure anatase TiO_2 (cf. Table 1). The volume of the Ge@Ti systems were found to contract by 0.2 and 0.4% for GGA and GGA + U calculations with respect to pure anatase, respectively, indicating that substitutional Ti replacement by Ge induces a lattice contraction. The local GeO_6 octahedron (cf. Figure 1) becomes inward-contracted so that the four equivalent Ge-O bonds (denoted by the B in Figure 1) become shorter than the corresponding Ti-O bond lengths (1.916 versus 1.938 Å for GGA calculations, and 1.929 versus 1.979 Å for the GGA + U case), while the two apical Ge-O bonds lengths (denoted by A) become significantly shorter than the corresponding Ti-O bonds lengths (1.905 versus 1.988 Å for the GGA calculations, and 1.906 versus 2.010 Å for the GGA + U case). The optimised geometrical structures from both methods indicate that the Ge dopants form a linear O-Ge-O unit with a short Ge-O distance. The Bader charge [59, 60] of the Ge was found to be +4e both for both techniques, suggesting that Ge^{4+} substitutes for Ti^{4+} (cf. Table 3). The calculated results were in qualitative agreement with experimental X-ray diffraction measurements [32], which reported a lattice contraction for substitutional replacement of Ti by Ge.

[insert Table 3 about here]

The optimised cell parameters of pure and Ge-doped rutile are summarised in Table 4. Both sets of results show that the Ge@Ti system volume contracted by 0.4 vs 0.7%

(GGA vs GGA + U) with respect to pure rutile. The Bader charge of the Ge atom was found to be +4e for both GGA and GGA + U method methods, suggesting that Ge^{4+} substitutes for Ti^{4+} (Table 4). These findings are consistent with the experimental observations of Ti replacement by Ge leading to lattice contraction [32]. The optimised local GeO_6 octahedron (cf. Figure 2) shows an inwardly shortened structure (Table 4): the four Ge-O bonds (denoted by B) are significantly shorter than those of the corresponding Ti-O bonds (1.916 vs 1.955 Å for the GGA calculations and 1.921 vs 1.991 Å for the GGA + U case). At the same time, the other two Ge-O bonds (denoted by A) are also shorter than those of the corresponding Ti-O bonds (1.933 vs 1.979 Å for the GGA calculations, and 1.937 versus 2.001 Å for the GGA + U case). The optimised local GeO_6 structure is different from that of the GeO_6 octahedron in Ge-doped anatase, and thus may lead to different electronic behaviour in Ge-doped anatase and rutile.

[insert Table 4 about here]

We found that the GGA band gap error in systems with and without Ge dopants is similar to the respective pure anatase and rutile; therefore, use of the GGA method is not affected by the underestimated band gaps, which is confirmed by GGA + U calculations. The calculated density of states (DOS) and projected DOS (PDOS) of Ge-doped anatase and rutile are shown in Figs. 5 & 6, respectively (left panel for GGA calculations and right panel for the GGA + U case). In pure anatase and rutile,

the valence band is composed mostly of O 2p states and the conduction band is dominated by Ti 3d states (cf. Figs. 3 & 4).

[insert Figs. 5 & 6 about here]

A study of the band gap and the density of states (DOS) of Ge-doped anatase and rutile may yield insights into the nature of how Ge affects electronic properties. It should be noted that the band gap of Ge-doped TiO_2 is essentially the energy separation between the O p-block and the Ti t_{2g}-block bands of pure anatase. For the Ge@Ti system, the contraction in the Ge-O bond length would be expected to shift the conduction band to lower energy regions, therefore reducing the band gap.

For Ge-doped anatase, the top of the valence band displays no obvious shift whilst the bottom of the conduction band was reduced significantly in energy (0.15 eV for GGA versus 0.07 eV for GGA + U) vis-à-vis pure anatase. This led to a concomitant reduction in the band gap, giving a red-shift in the optical absorption edge. Analysis of the PDOS showed that there were major Ge 4s states locating at energies below the host atoms' Ti 3d states. On the other hand, most of the Ge 4p states were found to lie deeper in the valence band. Therefore, it would not be expected that optical absorption would extend to the visible light region. However, the Ti 3d states move to lower energy region with respect to pure anatase, leading to a band gap reduction. These theoretical observations present a reasonable explanation for the experimental band gap reduction in the case of substitutionally Ge-doped anatase [32].

For Ge-doped rutile, the DOS (cf. Fig. 6a) shows similar results with Ge-doped anatase. In particular, the top of the valence band exhibited no movement and the bottom of the conduction band shifted to the lower energy region. This resulted in band gap narrowing relative to pure rutile (0.26 eV for GGA calculations and 0.09 eV for the GGA + U method), leading to a red-shift of the optical absorption edge. Furthermore, band gap narrowing is more obvious than that of Ge-doped anatase. Hence, it is reasonable to suggest that doping by Ge into rutile may extend to longer wavelengths in the visible light region. Analysis of the PDOS (cf. Fig. 6b) indicates that the microscopic mechanism is different from Ge-doped anatase, in which the Ge 4s impurities states are located at of the conduction band edge rather than lying deep in the conduction band. This band gap reduction is driven directly by Ge 4s impurities states in Ge-doped rutile. The different electronic behavior of Ge dopants in anatase and rutile arise possibly from the different GeO_6 local geometrical structures.

The ability of a semiconductor to undergo photoexcited electronic transitions for adsorbed dopants on its surface is dominated by the position of its valence band maximum (VBM) and conduction band minimum (CBM), and the redox potentials of the adsorbate. The closer the CBM energy to the vacuum level, the stronger the reducing power. Conversely, the lower the VBM energy, the higher the oxidizing power. For spontaneous production through photoelectrochemical (PEC) water-splitting process, the oxygen and hydrogen reactions must lie between the VBM and CBM. Thermodynamically, the VBM of TiO_2 needs to be below the water oxidation level and the CBM needs to be above the hydrogen production level. To

compare the photocatalytic activity of the Ge-doped TiO_2, we calculated the positions of the VBM and CBM of pure and doped systems with the GGA and GGA + U methods. Here, the scissors operator was set to 1.2 and 1.3 eV for GGA calculation (0.36 and 0.62 eV for GGA + U) for anatase and rutile, respectively, accounting for the difference between the experimental band gaps (3.2 eV for anatase and 3.0 eV for rutile) and the respective calculated band gaps of 2.0 and 1.7 eV for GGA calculations (2.84 and 2.38 eV for the GGA + U method). The results are presented in Figures 5 and 6, where the VBM and CBM of pure TiO_2 with respect to the normal hydrogen electrode (NHE) potential were taken from the experimental values [40].

Fig. 7 depicts the CBM and VBM of Ge-doped anatase (left panel) and rutile (right panel) with the GGA method. For Ge-doped anatase (left panel), Fig. 7 shows that the VBM has no shift and the CBM is lowered by about 0.15 eV with respect to pure anatase. At the same time, Fig. 7 (right panel) shows that the VBM of Ge-doped rutile is the same as that of pure rutile, and the CBM shifts to a lower energy of about 0.26 eV. In particular, the positions of the CBM and VBM straddle the water redox potential levels and the band gap narrows, suggesting that Ge-doped TiO_2 may be a very promising photocatalyst for water splitting under visible light. Therefore, it is recommended that further experiments be performed to investigate decomposition of organic matter and the photocatalytic activity of Ge-doped TiO_2.

[insert Fig. 7 about here]

Bi/S Doping

To determine the relative stability of the doped systems, we calculated the formation energy. The formation energies of substitutional S, Bi, and Bi/S dopants were calculated by

$$E_{form} = E(doped) - E(pure) - \mu_S - \mu_{Bi} + \mu_O + \mu_{Ti} \quad (1)$$

where $E(doped)$ is the total energy of the supercell containing the S, Bi, or Bi/S impurities, and $E(pure)$ is the total energy of the host pure TiO_2 supercell. μ_S and μ_{Bi} are the chemical potentials of impurity S and Bi, respectively. μ_O (μ_{Ti}) is the chemical potential for O (Ti). It should be noted that the formation energy is not fixed but depends on the growth conditions, which can be varied from Ti-rich to O-rich. For TiO_2, the chemical potentials of O and Ti satisfy the relationship $\mu_{Ti} + 2\mu_O = \mu(TiO_2)$. Under O-rich growth conditions, the chemical potential μ_O is determined by the energy of an O_2 molecule ($\mu_O = \mu(O_2)/2$) and μ_{Ti} is determined by the formula above. Under Ti-rich conditions, μ_{Ti} amounts to the energy of one Ti atom in bulk Ti ($\mu_{Ti} = \mu_{Ti}^{metal}$) and then μ_O is calculated on the basis of the previous formula. For S and Bi impurities, the chemical potentials μ_S are determined by $\mu_S = \mu(SO_2) - 2\mu_O$. μ_{Bi} is found based on consideration of Bi_2O_3 (space group: P211/C1), using the relationship $2\mu_{Bi} = \mu(Bi_2O_3) - 3\mu_O$. The calculated formation energies are summarized in Table 5; many of these results have been provided in our earlier work [36]. Study of these results suggests that: 1) S prefers to occupy O sites under Ti-rich growth condition; 2) the incorporation of S promotes that of Bi under Ti-rich conditions. Therefore, the synthesis of Bi/S-doped TiO_2 is more favourable in

comparison to single-Bi doping under the Ti-rich growth conditions experimentally [35], although it still possesses a large formation energy. It should be noted that the large ionic radii of S^{2-} (1.84 Å) and Bi^{3+} (1.03 Å) would result in high formation energies [61]. Introduction of a large S (Bi) atom into the interstitial site of the lattice induces large strain in the lattice about the dopant, and movement of the adjacent atoms. Although atomic relaxation reduces the formation energy for interstitial dopant configurations, the formation energy still remains high with values of 8.48 eV for S and 17.10 eV for Bi under Ti-rich conditions; therefore, interstitial S (Bi) defects are not energetically stable under normal conditions. In particular, simultaneous location of both S and Bi at interstitial sites leads to an unfavourable formation energy of 25.41 eV. Wang et al. also claimed that Bi is at the Ti sites in the lattice in their experimental samples [35], while some researchers have suggested that S atoms were doped as anions to replace the lattice O atoms in TiO_2 [21]. We have also found that simultaneous location of Bi and S at the Ti sites results in large formation energies of 24.43 eV under O-rich growth conditions and a higher value of 29.43 eV under Ti-rich conditions, indicating that S acting as a cationic dopant can hinder incorporation of Bi into the lattice. Consequently, we only discuss electronic structures for Bi and S as cationic and anionic dopants, respectively.

[insert Table 5 about here]

To compare the modifications of band gap and the origin of the observed red-shift

in the absorption light edge with doping by different ions, we calculated the DOS and the PDOS. They are plotted in Fig. 8. The calculated band gap of pure anatase TiO_2 is 2.0 eV, as shown in Fig. 8a, which is similar to other theoretical results [19], but underestimates the experimental value of 3.20 eV, due to well-known limitations of DFT. The band gap was found to broaden to 2.02, 2.06, and 2.06 eV for S-, Bi-, and Bi/S-doped TiO_2, respectively. For S-doped anatase (cf. Fig. 8b), it is shown clearly that acceptor levels of the S 3p states are slightly localized above the VBM O 2p states, and mixed with them to a certain extent, while the CBM exhibits nearly no movement, leading to reduction in the band gap by 0.55 eV. This may be responsible for the experimentally observed red-shift in visible light absorption. Mixing between S 3p and O 2p states is a positive factor for transfer of carriers, as Asahi et al. emphasized [17]. The Bader charge on S was found to be -1.10 e, a reasonable result with substitutional doping of an S atom for an O atom. When one O atom was replaced by one S atom, three S-Ti bonds were observed to form. Two were of 2.170 Å in length and one was longer (2.350 Å), but both lengths were substantially larger than those of optimized lengths for O-Ti bonds in pure anatase (1.938 and 1.988 Å); this was due to the larger ionic radius of an S atom than that of an O atom. From Figs. 8b and 8b', the small peak on the upper edge of the valence band should be a bonding peak. The one at -0.5 eV is another bonding peak. It should be noted that longer bond lengths lead to weaker bond strengths as well as higher energy states. The two 2.17 Å bonds are σ-type between S 3p and Ti 3d, with a greater strength and lower energy level, while the single 2.350 Å bond possesses relatively weaker π-bond

characteristics, with a higher energy level. They are all components of the valence band in S-doped TiO_2.

[insert Fig. 8 about here]

For Bi-doped TiO_2, the Bader charge on Bi was calculated to be 3e, indicating that the oxidization state of Bi ion is Bi^{3+}. Before investigating the microscopic mechanism of alterations in band gap, it is necessary to analyse spin-related properties, because replacement of a Ti atom by Bi (having an odd number of electrons) introduces paramagnetic centres. Therefore, we plotted the spin density on the (100) plane for Bi-doped TiO_2 in Fig. 9a. In this case, the unpaired electron is almost distributed on the adjacent O atoms with p states whereas substitutional Bi itself possesses a relatively small spin density with its s state, indicating the formation of Bi-O species. Although the experimental study did not report this [35], it is speculated that the introduction of substitutional Bi into the TiO_2 lattice should result in paramagnetic species. The DOS and PDOS show that the Bi 6s impurity states lie below the CBM with the formation of mid-gap states (Figs. 8c and 8c'). However, the Fermi level E_F is above the Bi 6s gap states, indicating that the impurity states are fully occupied. The electron transition from Bi 6s states to the CBM is reduced by about 0.50 eV with respect to pure anatase, in agreement with the results for the reduction of the extent of the band gap to lie between the top of the Bi^{3+} 6s band and the bottom of the Ti^{4+} 3d band [62]. Thus the absorption spectra extend to longer

wavelengths so that lower energy photons can be absorbed for photo-excitation, as observed experimentally [35]. When one Bi atom substitutes for one Ti atom, six O-Bi bonds were observed to form. Two were of 2.217 Å in length, while four were shorter (2.117 Å). Similar to the analysis for S-doped TiO_2, it was found that they were Bi 6s-O 2p anti-bonding. This indicates that electrons in the valence band can be excited to impurity states in the band gap in S- and Bi-doped TiO_2, and excited subsequently to the conduction band by absorption of visible-light. It is also possible that the impurity states at the VBM or CBM could act to reduce recombination rates of photo-excited carriers. Therefore, the impurity states would serve to promote the enhancement of photocatalytic efficiency.

[insert Fig. 9 about here]

For Bi/S-doped TiO_2 (cf. Figs. 8d and 8d'), the concomitant appearance of impurity states above the VBM and below the CBM consists of S 3p and Bi 6s states, respectively. The Fermi level E_F is pinned to the tail of the Bi 6s states hybridised with S 3p, implying that the gap states are partially occupied. The distance between the acceptor S 3p levels and the donor levels above the E_F is 1.12 eV, which is largely responsible for the band gap reduction. The calculated results indicate clearly that S-Ti-O and O-Bi-Ti bonding lead to the presence of additional impurity states which can contribute to enhanced visible light absorption after the addition of Bi into S-doped TiO_2. In this case, the Bader charge of Bi is also 3 e but the value for S

increases to -1.69 e. This value is more negative by about 0.59 e vis-à-vis the single S-doped system, because of attraction of more electrons from Bi and the adjacent Ti atoms. In this case, the unpaired electron was centralized mainly on adjacent O atoms, while the Bi and S atoms had a relatively small spin density (cf. Fig. 9b). O atoms exhibit p state character while Bi shows s state character. Further, the spin density is much less around the S atom than those of the O atoms because 3p orbitals are relatively further from nuclei vis-à-vis 2p orbitals. In other words, the spin density is localized around O atoms while it somewhat delocalized around S atoms. Therefore, the S atom does not possess simple p orbital characteristics, suggesting that there is hybridization between S atom and Bi atom; this is confirmed by the subsequent DOS and PDOS calculated results (see below). For respective O and Ti replacement by S and Bi in the TiO_2 lattice, two S-Ti bonds and a single Bi-S bond were formed. Both of the S-Ti bonds lengths were 2.214 Å in length, while the S-Bi bond length was 2.543 Å, so that the average bond length was 2.324 Å; this is larger than the average S-Ti bond length of 2.23 Å in (single) S-doped TiO_2, moving the S 3p states to higher energies. In addition, four of the six Bi-O bonds lengths were 2.140 and 2.157 Å, while one was 2.205 Å and the longest was 2.543 Å; the average Bi-O bond length of 2.224 Å in the co-doped case was larger than that of the average Bi-O bond length in single Bi-doped TiO_2 (2.150 Å). Therefore, one would expect Bi 6s states to move to higher energies upon co-doping, which is confirmed by the calculated DOS and PDOS (cf. Figs. 8 c, c', d, d'). A large possible benefit of codoping is the reduction of carriers' recombination rates with respect to monodoping [34]. However, experiments

have reported that monodoping can act either to introduce recombination centers or to reduce the carrier mobility [63, 12]. In the case of codoping of Bi with S, the S atom modifies the valence band edge (characteristic of p-type doping), whereas the Bi atom modifies the conduction band (n-type doping). Given that the acceptor (S-dopant) and donor (Bi-dopant) states are both relatively shallow, they would serve to act as capture traps for photoexcited holes or electrons; their impurity energy levels near the VBM and CBM could reduce further the recombination rate of photoexcited carriers [64]. The Bi/S codoped system exhibits both shallow acceptor and donor states, and a much smaller separations between the S 3p and Bi 6s states vis-à-vis pure TiO_2. Tang et al have indicated that hybridization of impurity energy levels is favorable towards enhancing the lifetimes of photoexcited carriers [65, 66]; the observation in this study of hybridization between shallow Bi 6s and S 3p states suggests that separation between photoexcited electron-hole pairs would be enhanced further vis-à-vis monodoping. This suggests that Bi and S co-doping is highly beneficial for the separation of photo-excited electron-hole pairs, and would serve to enhance the photocatalytic activity of anatase under visible light.

To verify that the conclusions drawn from our calculations are not affected by underestimated band gaps in standard DFT GGA calculations, we have performed further GGA + U calculations for pure TiO_2 and Bi/S-doped TiO_2 [36]. A value of 6.3 was chosen for the U parameter, based on the study of Gai et al. [34], and this produced a very good band gap result of 3.14 eV for pure TiO_2, and both approaches yielded similar electronic properties, indicating that the GGA band gap differences in

systems with and without dopants are similar [36].

N/W Doping

The dopant formation energies for the N, W, or N/W impurity were calculated in the same way as eqn. (1), as detailed in our previous work [40]. μ_N was determined from $\mu_N = \mu(N_2)/2$ and μ_W is calculated from bulk metal tungsten ($\mu_W = \mu_W^{metal}$). The calculated formation energies are summarized in Table 6. Their order suggests that: 1) N occupies the O site preferentially under Ti-rich conditions; 2) W is substituted preferentially for Ti under O-rich conditions; 3) the incorporation of N promotes that of W under both Ti- and O-rich conditions. Therefore, the experimental synthesis of N/W-doped TiO_2 is more thermodynamically favourable vis-à-vis single W doping under Ti-rich conditions, due to a lower formation energy of 1.61 eV. Further, both single W doping and N/W-codoping are energetically favourable under O-rich conditions due to negative formation energies.

[insert Table 6 about here]

The DOS and PDOS are plotted in Fig. 10. The calculated band gap of pure anatase is 2.0 eV, as shown in Fig. 2a, which is similar to other theoretical results [19], but underestimates the experimental value of 3.20 eV, due to well-known limitations in DFT. However, in this study, we focus on changes in the band gap upon doping, so the GGA method is expected to largely cancel the band gap error between different

systems. Further, recent theoretical work focused on nonmetal codoping with transition metals has shown that standard DFT methods can deal fully with these doped systems [34]. For N-doped TiO_2 (Figs. 10b & f), an O atom is replaced by an N atom, leaving the system deficient by one electron. This implies that the N oxidation state is -2 rather than -3, and that its 2p states are not fully occupied, giving the N atom a doublet spin state. It is clear in Fig. 10 that N 2p states are localized in the band gap without altering the VBM and CBM vis-à-vis the undoped case. The electron in the valence band can be excited into gap states and then subsequently to the conduction band by visible-light absorption, suggesting that gap-to-conduction band transitions are responsible for red shifts in the absorption edge. Conversely, emptied N 2p states can act as traps for excited electrons, which can serve to promote electron-hole recombination rates. Therefore, the photocatalytic activity of N-doped TiO_2 is more limited in the visible light region. For W-doped TiO_2 (Figs. 10c & g), the impurity states lie below the CBM, indicating that W 5d states are below host Ti 3d states. This led to a band gap reduction by about 0.2 eV. These states would be expected to lead to enhancements in photocatalytic efficiency. Indeed, doping by W may also be responsible for red-shifts in optical absorption edges observed experimentally [15, 16]. Figs. 10a & e shows that the valence band edge consists mainly of O 2p states, whereas the conduction band edge has predominately Ti 3d states. Therefore, codoping with N and W would be expected to modify the conduction and valence band edges simultaneously because N has a different atomic p orbital energy relative to O, and W has a different atomic d orbital energy vis-à-vis Ti.

For N/W-doped TiO_2 (Figs. 10d & h), it is interesting that a hybridised state (composed of N 2p orbitals and W 5d states) is formed; in particular, the hybridised states are located mainly at the edge of the valence band whereas other W 5d states are at the edge of the conduction band. The W 5d states may contribute to the lowering of the energy levels of the N 2p states, bringing the N states closer to the valence band, and therefore enhancing mixing of N 2p and O 2p states in the valence band. In this case, the isolated states disappear and a continuum is formed. Conversely, the position of W 5d states were pushed to lower energy regions due to the interaction between W 5d and N 2p states, which led to a 0.5 eV reduction of the N/W band gap vis-à-vis pure TiO_2. It is clear that the addition of W to N-doped TiO_2 changes the character of N 2p orbitals from isolated midgap states to N 2p states mixed with O 2p states. As electrons move from occupied W 5d states to empty lower energy 2p states (N^{2-} impurities), this indicates that N^{2-} ion (doublet) states transfer into N^{3-} ion (singlet) states, filling the 2p band. These results indicate clearly that N-W-O bonding leads to the formation of additional impurity states which can contribute to enhanced visible light absorption upon addition of W to N-doped TiO_2.

[insert Fig. 10 about here]

To study further the variation of N 2p impurity states with different behavior in the same N doping content in N- and N/W-doped TiO_2, we have plotted the total charge and spin density in Fig. 11. The inclusion of an N atom in the lattice results in a

paramagnetic impurity and a doublet ground state. The unpaired electron has a strong N 2p character, and is largely localized on the N atom (Fig. 11a), with the spin density centered fully there (Fig. 11b). For N/W-doped TiO_2, however, the electron density is more localized on the N than W atom (Fig. 11c) while the spin density is very small and significantly dispersed. This shows that the spin density of an N atom couples with that of the adjacent W, resulting in hybridisation of the N 2p with W 5d states (Figs. 10d & 11d]. This indicates that N forms a stable eight-electron shell with no unpaired electron because of Ti^{4+} replacement by W^{+6}. Bader charges are summarised in Table 7. They shows that the N ion has a charge of -1.37 |e| for N-doping, while it is -2.01 |e| for N/W-doping, with more electrons transferring from the W and adjacent Ti atoms to the N ion; this implies that the unpaired electron of N leads to the formation of a new bond with W. The bond length of N-W is 1.851 Å, which is much shorter than that of the N-Ti length of 2.026 Å for N-doping. This indicates further that a strong N-W bond forms in N/W-codoped TiO_2. These findings helps to rationalise experimental reports of W doping leading to red-shifts in the optical absorption edge [15, 16] and N/W-codoping enhancing the absorption region and photocatalytic activity [38, 39].

[insert Table 7 and Fig. 11 about here]

Conclusions

We have used the PBE and Perdew-Wang exchange-correlation approaches to

predict the band gap of pure anatase and rutile. The PBE method is in closer agreement with experiment, mirroring the reasonable performance noted by Lazzeri et al. [42], but still underestimates the band gap. The use of the GGA+U method for the Perdew-Wang functional resulted in a clear improvement in band gap prediction. Although tight-binding methods have resulted in good band gap estimates in titania [10], the present study has shown that the GGA+U technique offers improved band gap predictive performance, at the slight expense of prediction of lattice parameters. Further tuning of the Hubbard U parameter may lead to an optimal band gap prediction. In any event, DFT methods in general are still relatively inaccurate for the prediction of band gap properties in complex metal oxide systems. Although it is clear that the use of semi-empirical corrections (e.g., DFT+U approaches) may aid in improving the prediction of these properties, this was at the expense of structural properties in the case of pure titania in this particular study. This remains a challenge for DFT in metal oxide systems, although the increasing use of exact exchange approaches with hybrid functionals is showing promise of offering more quantitative accuracy for band gap properties without compromising the structural description, despite the greater computational requirements.

For Ge-doped anatase and rutile, both GGA and GGA + U methods lead to lattice contraction, although the GGA results are better than those of GGA + U. The calculated electronic properties demonstrate that band gap narrowing occurred (by 0.15 eV with GGA and 0.07 eV with GGA + U) in anatase due to the host Ti 3d states moving to lower energies. On the other hand, the Ge 4s impurities states are situated

at the conduction band edge and lead to band gap narrowing (0.26 eV with GGA and 0.09 eV with GGA + U) in rutile TiO_2. From the calculated DOS, it is predicted that Ge-doped anatase and rutile TiO_2 have suitable positions of band edges, which can be investigated further as promising photocatalysts for overall water splitting under visible light.

For Bi/S doping in anatase, single S doping reduces the band gap, driven by mixing of S 3p and O 2p states, while single Bi ion doping produces midgap states which we suggest may be responsible for the experimentally observed red-shift of the optical absorption edge. In particular, our calculations suggest that Bi and S co-doping can reduce the band gap and enhance photocatalytic activity under visible light; shallow acceptor S 3p states and shallow donor Bi 6s states hybridised with S 3p were produced within the band gap, which serve to enhance the separation of electron-hole pairs excited by photon irradiation. This could lead to substantial enhancements in photocatalytic activity of TiO_2 under visible-light, in agreement with recent experimental findings.

N and W codoping in anatase can reduce the band gap effectively and enhance photocatalytic activity under visible light irradiation. The hybridisation between N 2p and W 5d states leads to strong mixing of N 2p and O 2p states, leading to the formation of continuum states. At the same time, W 5d states were located at the conduction band edge. Both of these factors led to band gap reduction, rationalizing experimental observations of enhanced photocatalytic activity.

Acknowledgements

This work was supported by the Irish Research Council for Science, Engineering and Technology. N.J.E. thanks the Ireland Canada University Foundation for a research visit grant. The authors thank Dr. Michelle Shaw and Mr. Ritwik Kavethekar for useful discussions, and Science Foundation Ireland and the Irish Centre for High End Computing for the provision of computational resources.

References

[1] A. L.Linsebiger, G. Q. Lu, J. T.Yates, Photocatalysis on TiO2 Surfaces: Principles, Mechanisms, and Selected Results， Chem. Rev. 95, 735-758 (1995).

[2] A. Fujishima, K.Honda, Electrochemical Photolysis of Water at a Semiconductor Electrode, Nature 28, 37-38 (1972).

[3] R. Sanjines, H. Tang, H. Berger, F. Gozzo, G. Margaritondo and F. Levy, Photoemission spectromicroscopy was used to investigate the electronic structure of TiO_2, *J. Appl. Phys.* 1994, 75:2945-2951.

[4] J. Pascual, J. Camassel and H. Mathieu, Fine structure in the intrinsic absorption edge of TiO_2 ,*Phys. Rev. B* 1978, 18:5606-5614.

[5] Herrmann, J. M.; Disdier, J.; Pichat, P. Effect of chromium doping on the electrical and catalytic properties of powder titania under UV and visible illumination, *Chem. Phys. Lett.* 1984, *108*, 618-622.

[6] Choi, W.; Termin, A.; Hoffmann, M. R. The Role of Metal Ion Dopants in Quantum-Sized TiO2: Correlation between Photoreactivity and Charge Carrier Recombination Dynamics*J. Phys. Chem.* 1994, *98*, 13669-13679.

[7] Yamashita, Y.; Ichiashi, M.; Taeuchi, S.; Kishiguchi, M.; Anpo, J. Characterization of metal ion-implanted titanium oxide photocatalysts operating under visible light irradiation *Synchrotron Radiat.* 1999, *6*, 451-452.

[8] Breckenridge, R. G.; Hosler, W. R. Electrical Properties of Titanium Dioxide Semiconductors, *Phys. Rev.* 1953, *91*, 793-802.

[9] Cronemeyer, D. C. Infrared Absorption of Reduced Rutile TiO_2 Single

Crystals ,*Phys. Rev.* 1959, *113*, 1222-1226.

[10] H. Wang and J.P. Lewis, Second-generation photocatalytic materials: anion-doped TiO_2 *J. Phys.: Condens. Matter* 2006, 18:421-434, and references therein.

[11] Dudarev, S. L.; Botton, G. A.; Savarsov, S. Y.; Humphreys, C. J.; Sutton, A. P. An Electron-energy-loss spectra and the structural stability of nickel oxide: LSDA+U study ,*Phys. Rev. B* 1998, *57*, 1505-1509.

[12] J. M.Herrmann, J. Disdier, P. Pichat, Effect of chromium doping on the electrical and catalytic properties of powder titania under UV and visible illumination,Chem. Phys. Lett. 108, 618-622 (1984).

[13] W.Choi, A. Termin, M. R. Hoffmann, The Role of Metal Ion Dopants in Quantum-Sized TiO2: Correlation between Photoreactivity and Charge Carrier Recombination Dynamics J. Phys. Chem. 98, 13669-13679 (1994).

[14] N. Couselo, F. G. García, R. J. Candal, M. J. Jobbágy, Tungsten-Doped TiO_2 vs Pure TiO_2 Photocatalysts: Effects on Photobleaching Kinetics and MechanismJ. Phys. Chem. C 112, 1094-1100 (2008).

[15] Y. Yang, H. Y. Wang, X. Li, C. Wang, Electrospun mesoporous W^{6+}-doped TiO_2 thin films for efficient visible-light photocatalysisMater. Lett. 63, 331-333 (2009).

[16] R. Long, Y. Dai, B. B. Huang, Geometric and Electronic Properties of Sn-Doped TiO_2 from First-Principles Calculations J. Phys. Chem. C 113, 650-653 (2009).

[17] R. Asahi, T. Morikawa, T. Ohwaki, K. Aoki, Taga, Y. Visible-Light Photocatalysis in Nitrogen-Doped Titanium Oxides Science 293, 269-271 (2001).

[18] H. Irie, Y. Watanabe, K. Hashimoto, Nitrogen-Concentration Dependence on Photocatalytic Activity of $TiO_{2-x}N_x$ Powders J. Phys. Chem. B 107, 5483-5486 (2003).

[19] T. Umebayashi, Y. Yamaki, H. Itoh, K. Asai, Band gap narrowing of titanium dioxide by sulfur doping Appl. Phys. Lett. 81, 454 (2002).

[20] D. Chen, D. Yang, Q. Wang, Y. Jiang, Effects of Boron Doping on Photocatalytic Activity and Microstructure of Titanium Dioxide NanoparticlesInd. Eng. Chem. Res. 45, 4110-4116 (2006).

[21] Umebayashi, T.; Yamaki. Y.; Yamamoto, S.; Miyashita, A.; Tanaka, S.; Asahi, K. Sulfur-doping of rutile-titanium dioxide by ion implantation: Photocurrent spectroscopy and first-principles band calculation studies*J. Appl. Phys.* 2003, *93*, 5156-5161.

[22] Li, H. X.; Zhang, X. Y.; Huo, Y. N.; Zhu, J. Supercritical Preparation of a Highly Active S-Doped TiO_2 Photocatalyst for Methylene Blue Mineralization *Environ. Sci. Technol.* 2007, *41*, 4410-4414.

[23] Grey, I. E.; Li, C.; Macrae, C. M.; Bursill, L. A. Boron Incorporation into Rutile. Phase Equilibria and Structure Considerations*J. Solid State Chem.* 1996, *127*, 240-247.

[24] Sakthivel, S.; Kisch, H. Daylight Photocatalysis by Carbon-Modified Titanium Dioxide *Angew. Chem., Int. Ed.* 2003, *42*, 4908-4911.

[25] Khan, S. U. M.; Al-Shahry, M.; Ingler, Jr. W. B. Efficient Photochemical Water Splitting by a Chemically Modified n-TiO_2 *Science* 2002, *297*, 2243-2245.

[26] Ohno, T.; Tsubota, T.; Nishijima, K.; Miyamoto, Z. Degradation of Methylene

Blue on Carbonate Species-doped TiO_2 Photocatalysts under Visible Light *Chem. Lett.* 2004, *33*, 750-751.

[27] Barborini, E.; Conti, A. M.; Kholmanov, I. N.; Miseri, P.; Podestå, A.; Milani, P.; Cepek, C.; Sakho, O.; Macovez, R.; Sancrotti, M. Nanostructured TiO2 Films with 2 eV Optical Gap *Adv. Mater.* 2005, *17*, 1842-1846.

[28] Lee, J. Y.; Park. J.; Cho, J. H. Electronic properties of N- and C-doped TiO_2 *Appl. Phys. Lett.* 2005, *87*, 011904-011906.

[29] Li, J.; Zeng, H. C. Hollowing Sn-Doped TiO_2 Nanospheres via Ostwald Ripening,*J. Am. Chem. Soc.* 2007, *129*, 15839-15847.

[30] Uchiyama, H.; Imai, H. Crystal growth of metastable rutile-type $Ti_xSn_{1-x}O_2$ solid solutions in an aqueous system *Chem. Commun.* 2005, *48*, 6014-6016.

[31] Long, R.; Dai, Y.; Huang, B. B. Geometric and Electronic Properties of Sn-Doped TiO_2 from First-Principles Calculations*J. Phys. Chem. C* 2009, *113*, 650-653.

[32] Long, R.; Dai, Y.; Guo, M.; and Huang. B. B. *Phys. Chem. Chem. Phys.* 2009, 11, 8165.

[33] Chatterjee, S.; Chatterjee, A. Optoelectronic Properties of Ge-Doped TiO_2 Nanoparticles *Jpn. J. Appl. Phys.* 2008, *47*, 1136-1139.

[34] Gai, Y. Q.; Li, J. B.; Li, S. S.; Xia, J. B.; Wei, S. H. Design of Narrow-Gap *TiO_2*: A Passivated Codoping Approach for Enhanced Photoelectrochemical Activity ,*Phys. Rev. Lett.* 2009, *102*, 036402-036405.

[35] Wang, Y.; Meng, Y. L.; Ding, H. M.; Shan, Y. K.; Zhao, X.; Tang, X. Z. A Highly

Efficient Visible-Light-Activated Photocatalyst Based on Bismuth- and Sulfur-Codoped TiO_2 *J. Phys . Chem. C* 2008, *112*, 6620-6626.

[36] R. Long; N.J. English, Synergistic Effects of Bi/S Codoping on Visible Light-Activated Anatase TiO_2 Photocatalysts from First Principles *J. Phys. Chem. C*, 113, 8373-8377 (2009).

[37] W. R. Duncan, O. V. Prezhdo, Temperature Independence of the Photoinduced Electron Injection in Dye-Sensitized TiO_2 Rationalized by Ab Initio Time-Domain Density Functional TheoryJ. Am. Chem. Soc. 130, 9756-9762 (2008).

[38] B. F. Gao, Y. Ma, Y. A. Cao, W. S. Yang, J. N. Yao, Great Enhancement of Photocatalytic Activity of Nitrogen-Doped Titania by Coupling with Tungsten Oxide J. Phys. Chem. B 110, 14391-14397 (2006).

[39] Y. F. Shen, T. Y. Xiong, T. F. Li, K. Yang, Tungsten and nitrogen co-doped TiO_2 nano-powders with strong visible light response ,Applied Catalysis B: Enviormental 83, 177-185 (2008).

[40] R. Long; N.J. English, First-principles calculation of nitrogen-tungsten codoping effects on the band structure of anatase-titania *Appl. Phys. Lett.*, 94(13), 132102-132104 (2009).

[41] J.P. Perdew, K. Burke, M. Ernzerhof, Generalized Gradient Approximation Made Simple, *Phys. Rev. Lett.* 1996, 77, 3865-3868.

[42] M. Lazzeri, A. Vittadini, and A.Selloni et al., Structure and energetics of stoichiometric TiO_2 anatase surfaces *Phys. Rev. B* 2001, *63*, 155409(1)-(9).

[43] M. Fuchs, M. Scheffler, Ab initio pseudopotentials for electronic structure

calculations of poly-atomic systems using density-functional theory, *Comput. Phys. Commun.* 1999, *119*, 67-98.

[44] J. Hutter, P. Ballone, M. Bernasconi, P. Focher, E. Fois, S. Goedecker, D. Marx, M. Parrinello and M. Tuckerman, CPMD 3.11.0, MPI für Festkörperforschung, Stuttgart and IBM Zurich Research Laboratory, 2006

[45] Perdew, J. P.; Wang, Y.; Accurate and simple analytic representation of the electron-gas correlation energy, *Phys. Rev. B* 1992, *45*, 13244-13249.

[46] Kresse, G.; Hafner, J. *Ab initio* molecular-dynamics simulation of the liquid-metal–amorphous-semiconductor transition in germanium ,*Phys. Rev. B* 1994, *4*9, 14251-14269.

[47] Kresse, G.; Furthermüller, J. Efficient iterative schemes for *ab initio* total-energy calculations using a plane-wave basis set, *Phys. Rev. B* 1996, *54*, 11169-11186.

[48] Monkhorst, H. J.; Pack, J. D. Special points for Brillouin-zone integrations ,*Phys. Rev. B* 1976, *13*, 5188-5192.

[49] Davidson, E. R. *Methods in Computational Molecular Physics* edited by G.H.F. Diercksen (Reidel, Dordrecht, 1983)

[50] Wilson, S. Vol. 113 *NATO Advanced Study Institute, Series C;* Plenum, New York, 1983; p 95.

[51] Anisimov, V. I.; Zaanen, J.; Andersen, O. K. Band theory and Mott insulators: Hubbard *U* instead of Stoner *I* ,*Phys. Rev. B* 1991, *44*, 943-954.

[52] Bocquet, A .E.; Mizokawa, T.; Morikawa, K.; Fujimori, A.; Barman, S.; Maiti, R. K.; Sarma, D. D.; Tokura, Y.; Onoda, M. Electronic structure of early

3*d*-transition-metal oxides by analysis of the 2*p* core-level photoemission spectra ,*Phys. Rev. B* 1996, *53*, 1161-1170.

[53] Okada, K.; Uozumi, T.; Kotani, A. Split-Off State Formation in the Final State of Photoemission in Ti Compounds, *J. Phys. Soc Jpn.* 1994, *63*, 3176-3184.

[54] Uozumi, T.; Okada, K.; Kotani, A. Electronic Structures of Ti and V Oxides: Calculation of Valence Photoemission and Bremsstrahlung Isochromat Spectra *J. Phys. Soc. Jpn.* 1993, *62*, 2595-2599.

[55] Tanaka, A.; Jo, T. Resonant 3*d*, 3*p* and 3*s* Photoemission in Transition Metal Oxides Predicted at 2*p* Threshold,*J. Phys. Soc. Jpn.* 1994, *63*, 2788-2807.

[56] Calzado, C. J.; Hernánda, N. C.; Sanz, J. F. Effect of on-site Coulomb repulsion term *U* on the band-gap states of the reduced rutile (110) TiO_2 surface, *Phys. Rev. B* 2008, *77*, 045118-1-10.

[57] Yang, K.S.; Dai, Y.; Huang, B. B.; Whangbo, M. H. Density Functional Characterization of the Visible-Light Absorption in Substitutional C-Anion- and C-Cation-Doped TiO_2 ,J. Phys. Chem. C 2009, 113 2624-2629.

[58] Burdett, J. K.; Hughbandks, T.; Miller. G. J. J.; Richardson, W. Smith, J. Structural-electronic relationships in inorganic solids: powder neutron diffraction studies of the rutile and anatase polymorphs of titanium dioxide at 15 and 295 K, *J. Am. Chem. Soc.* 1987, *109*, 3639-3646.

[59] Henkelman, G.; Arnaldsson, A.; Jónsson, H.; A fast and robust algorithm for Bader decomposition of charge density, *Comput. Mater. Sci.* 2006, *36*, 354-360

[60] Sanville, E.; Kenny, S. D.; Smith, R.; Henkelman, G. Improved grid-based

algorithm for Bader charge allocation*J. Comp. Chem.* 2007, *28*, 899-908.

[61] *CRC Handbook of Chemistry and Physics 87th Edition*, edited by David R. Lide (Taylor & Franics, London, 2006).

[62] Rengaraj, S.; Li, X. Z.; Tanner, P. A.; Pan, Z. F. Pang, G. K. H. Photocatalytic degradation of methylparathion—An endocrine disruptor by Bi^{3+}-doped TiO_2, *J. Mol. Catal. A: Chem.* 2006, *247*, 36-43.

[63] Irie, H.; Watanabe, Y. Hashimoto, K. Carbon-doped Anatase TiO_2 Powders as a Visible-light Sensitive Photocatalyst *Chem. Lett.* 2003, *32*, 772-773.

[64] Zhao, Z. Y.; Liu, Q. J. *Catal. Lett.* Designed Highly Effective Photocatalyst of Anatase TiO_2 Codoped with Nitrogen and Vanadium Under Visible-light Irradiation Using First-principles 2008, *124*, 111-117.

[65] Tang, J.; Zou, Z.; Ye, J. Photocatalytic Decomposition of Organic Contaminants by Bi2WO6 Under Visible Light Irradiation, *Catal. Lett.* 2004, 92, 53-56.

[66] Tang, J.; Ye, J. Photocatalytic and photophysical properties of visible-light-driven photocatalyst $ZnBi_{12}O_{20}$,*Chem. Phys. Lett.* 2005, 410, 104-107.

TABLE 1: Optimised lattice parameters and bond length of anatase (Å).

	GGA	GGA+U
a=*b*	3.800 (3.782[a])	3.888
c	9.483 (9.502[a])	9.522

[a]ref. 58

TABLE 2: Optimised lattice parameters and bond lengths of rutile (Å).

	GGA	GGA+U
a=*b*	4.608 (4.587[a])	4.648
c	2.957 (2.954[a])	3.042

[a]ref. 58

TABLE 3: Optimised Lattice Parameters and bond length of Ge-doped anatase. The calculated Bader charge of Ge and its adjacent six O atoms are also specified. The numbers in parenthesis refer to the numbers of O atoms.

	GGA	GGA+U
	Ge@Ti	Ge@Ti
a=b	3.795	3.877
c	9.490	9.532
Volume ($Å^3$)	546.59	572.97
ratio	0.2%	0.4%
A (Å)	1.905	1.906
B (Å)	1.916	1.929
Charge (|e|), Ge	4	4
O	-1.55(6); -1.59(2)	-1.56(4)

[a]ref. 58

TABLE 4: Optimised Lattice Parameters of Ge-doped Rutile. The calculated Bader charge of Ge and its adjacent six O atoms are also specified. The numbers in parenthesis refer to the number of O atoms.

	GGA	GGA+U
	Ge@Ti	Ge@Ti
a=b	4.599	4.635
c	2.956	3.019
Volume ($Å^3$)	500.11	521.73
ratio	0.4%	0.7%
A (Å)	1.933	1.937
B (Å)	1.916	1.921
Charge (|e|), Ge	4	4
O	-1.53(3) -1.57(2) -1.59(1);	-1.57(3) -1.59(2) -1.61(1)

[a]ref. 58

TABLE 5. Formation energies E_{form} for S-, Bi-, and Bi/S-doped anatase, in eV.

		Ti-rich	O-rich
E_{form}	*S-doped*	*-5.12*	*9.88*
E_{form}	*Bi-doped*	*11.26*	*8.76*
E_{form}	*Bi/S-doped*	*5.29*	*17.79*

TABLE 6. Formation energies (eV) E_{form} for N-, W-, and N/W-doped anatase, in eV.

		Ti-rich	O-rich
E_{form}	*N-doped*	*0.90*	*5.90*
E_{form}	*W-doped*	*3.40*	*-6.60*
E_{form}	*N/W-doped*	*1.61*	*-3.39*

TABLE 7. Bader Charges (|e|) on dopant atoms and their adjacent atoms in N-, W-, and N/W-doped anatase. The numbers in parenthesis represent the numbers of atoms.

	N-doped	W-doped	N/W-doped
N	*-1.37*		*-2.01*
W		*4.59*	*4.63*
O		*-1.47(2), -1.49(2), -1.58(2)*	*-1.36(2), -1.49, -1.55 (2)*
Ti	*2.63(3)*		*2.60(2)*

Figure Captions

Figure 1. View of the 48-atom (2 × 2 × 1) supercell used for substitutional replacement of Ti by Ge in anatase TiO_2, denoted by Ge@Ti. The local structure of GeO6 octahedron is described according to the two parameters A and B. The large grey spheres represent Ti atoms, while the small dark spheres denote O atoms and the large dark sphere represents the Ge atom.

Figure 2. View of the 48-atom (2 × 2 × 2) supercell used for replacement of Ti by Ge in rutile TiO_2, denoted by Ge@Ti. The local structure of GeO6 octahedron is described according to the two parameters A and B. The large grey spheres represent Ti atoms, while the small dark spheres denote O atoms and the large dark sphere represents the Ge atom.

Figure 3. (A) Density of states for anatase by GGA calculations using the PAW approach. (B) Density of states for anatase by GGA + U calculations using the PAW approach. The top of valence band of anatase is taken as the reference level.

Figure 4. (A) Density of states for rutile by GGA calculations using the PAW approach. (B) Density of states for rutile by GGA + U calculations using the PAW approach. The top of valence band of rutile is taken as the reference level.

Figure 5. (A) Density of states for (a) Ge@Ti anatase by GGA calculations. (B)

Density of states for (a) Ge@Ti anatase via the GGA + U approach. The corresponding projected density of states (PDOS) are shown in (b). The top of valence band of pure anatase is taken as the reference level.

Figure 6. (A) Density of states for (a) Ge@Ti rutile by GGA calculations. (B) Density of states for (a) Ge@Ti rutile via the GGA + U technique. The corresponding projected density of states (PDOS) are shown in (b). The top of valence band of pure rutile is taken as the reference level.

Figure 7. Comparison of the calculated VBM and CBM positions (versus the normal hydrogen electrode (NHE) potential) of Ge-doped anatase (left panel) and rutile (right panel) TiO_2 from GGA calculation with the corresponding experimental values of the pure cases.

Figure 8. (A) The density of states (DOS) for each of the Bi/S-doped systems. (B) The projected density of states (PDOS). The top of valence band of pure anatase is taken as the reference level. The dashed lines represent the Fermi level, E_F.

Figure 9. Spin density maps on the (100) plane for (a) Bi-doped TiO_2 and (b) Bi/S-doped TiO_2.

Figure 10. DOS (left) for (a) pure TiO_2, (b) N-doped TiO_2, (c) W-doped TiO_2, and (d)

N/W-doped TiO_2. The corresponding PDOS are shown on the right in (e)-(h). The PDOS plots of (f)-(h) are enlarged for clarity. The top of valence band of pure TiO_2 is taken as the reference level.

Figure 11. Electron densities (left) and spin densities (right). (a), (b) for N-doped TiO_2 and (c), (d) for N/W-doped TiO_2.

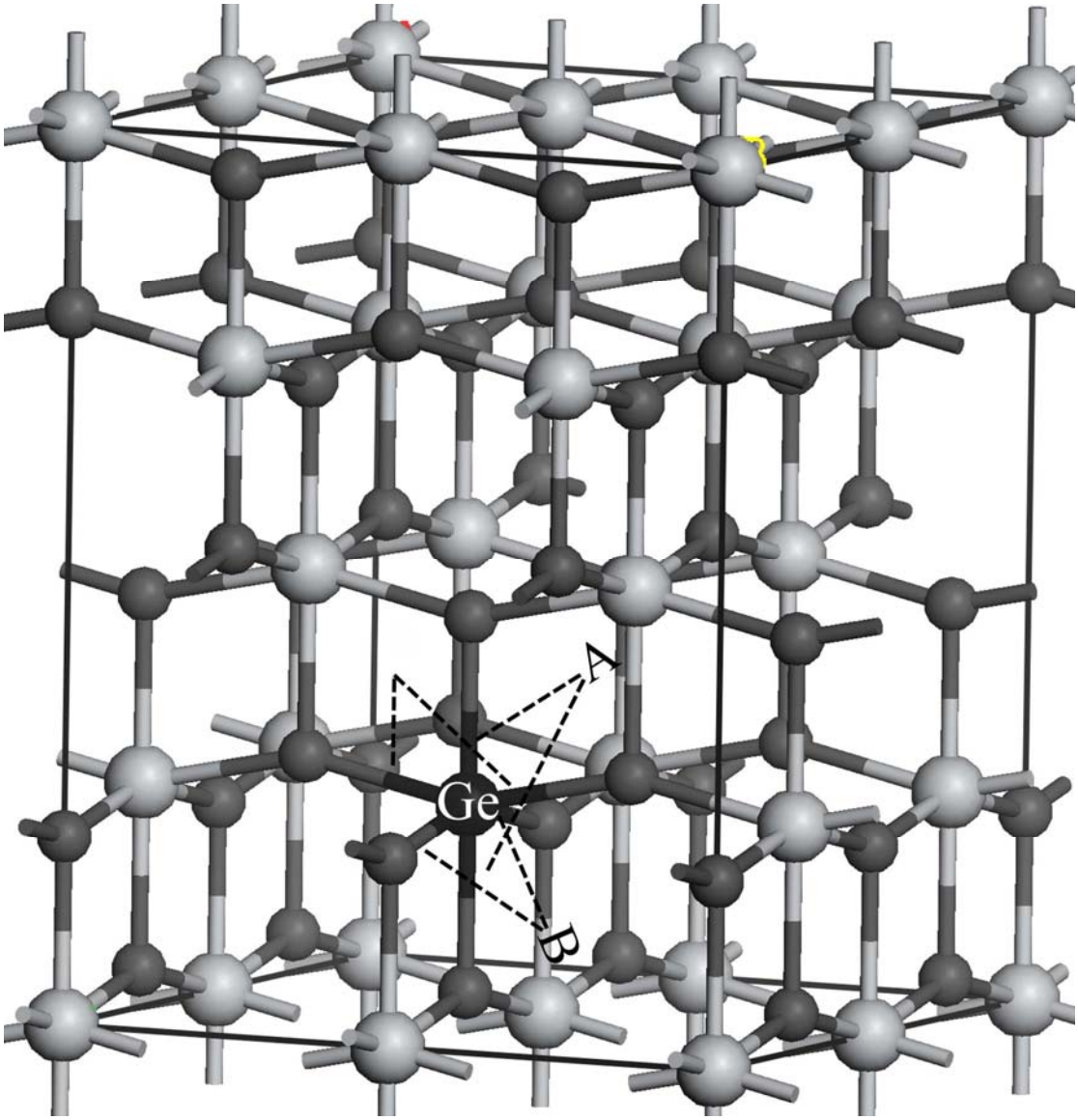

Figure 1

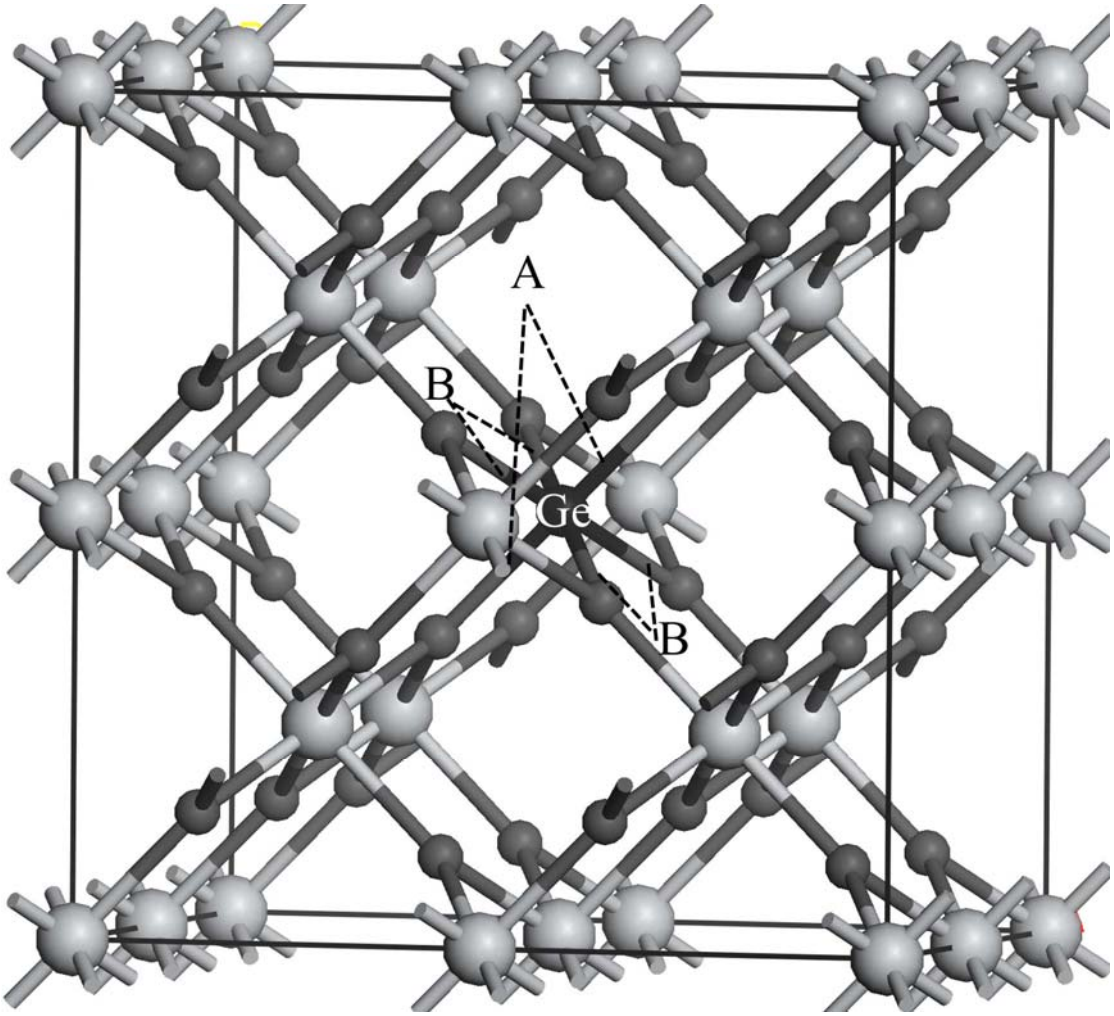

Figure 2

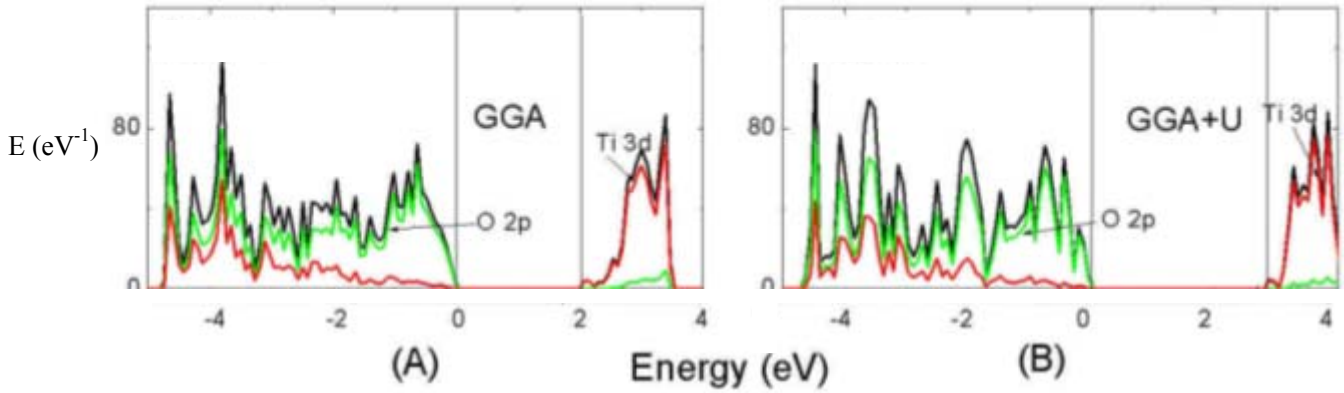
E (eV-1)
80
0
GGA
Ti 3d
O 2p
-4
-2
0
2
4
(A)
Energy (eV)
80
0
GGA+U
Ti 3d
O 2p
-4
-2
0
2
4
(B)

Figure 3

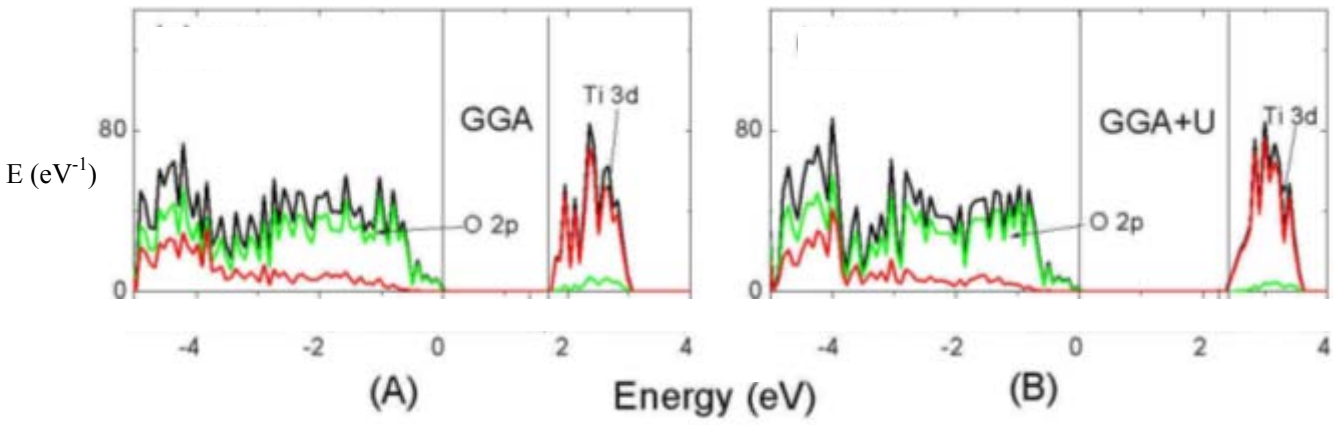

Figure 4

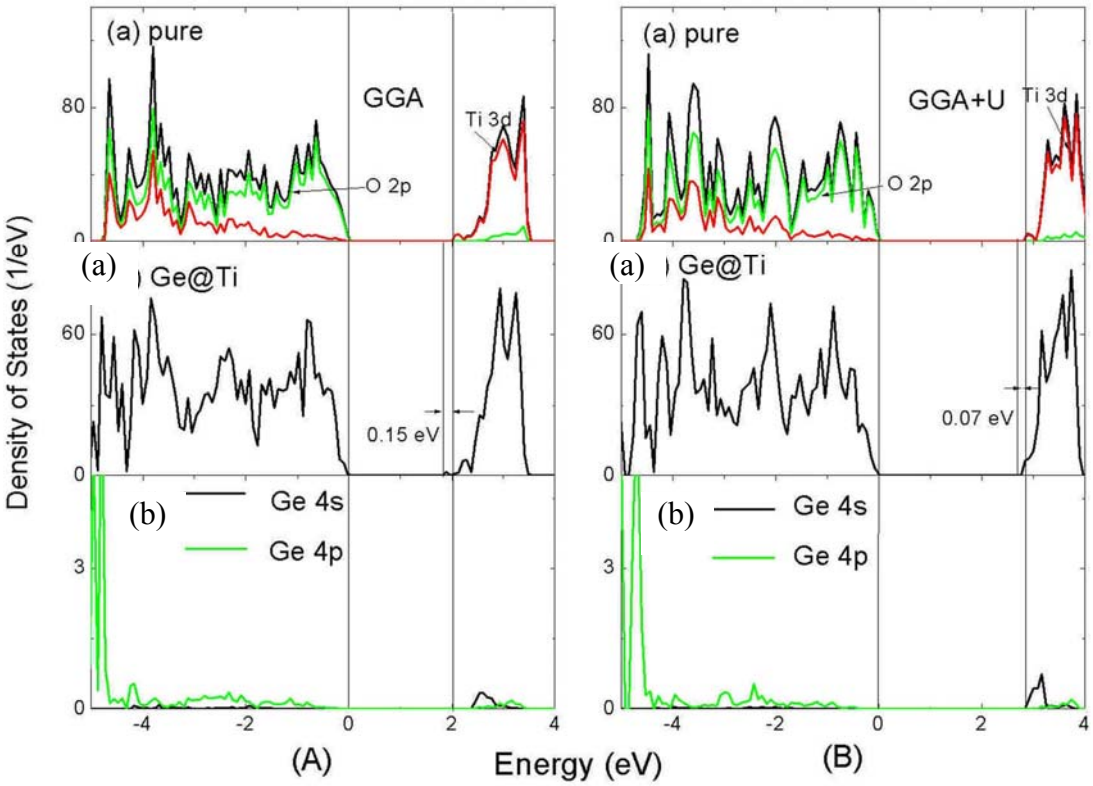
(a) pure
GGA
Ti 3d
O 2p
(a) Ge@Ti
0.15 eV
(b)
Ge 4s
Ge 4p
(A)
(a) pure
GGA+U
Ti 3d
O 2p
(a) Ge@Ti
0.07 eV
(b)
Ge 4s
Ge 4p
(B)
Density of States (1/eV)
Energy (eV)

Figure 5

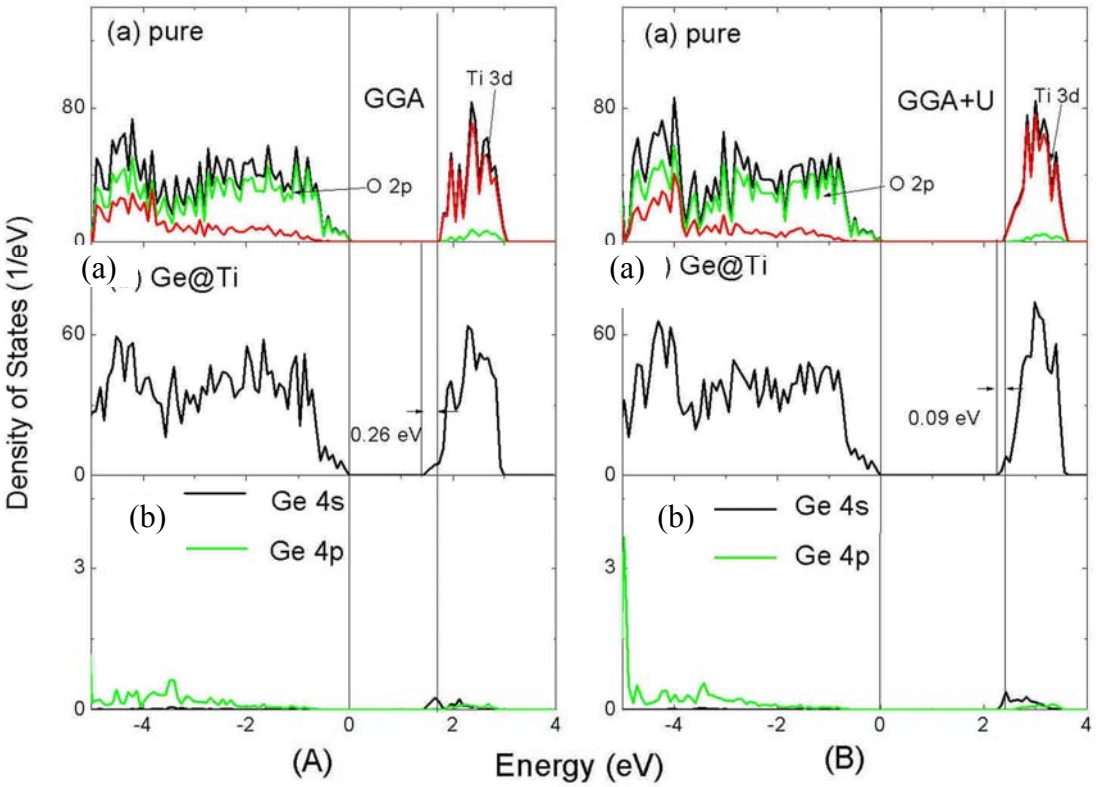
(a) pure
GGA
Ti 3d
O 2p
(a) Ge@Ti
0.26 eV
(b)
Ge 4s
Ge 4p
(A)
(a) pure
GGA+U
Ti 3d
O 2p
(a) Ge@Ti
0.09 eV
(b)
Ge 4s
Ge 4p
(B)
Density of States (1/eV)
Energy (eV)

Figure 6

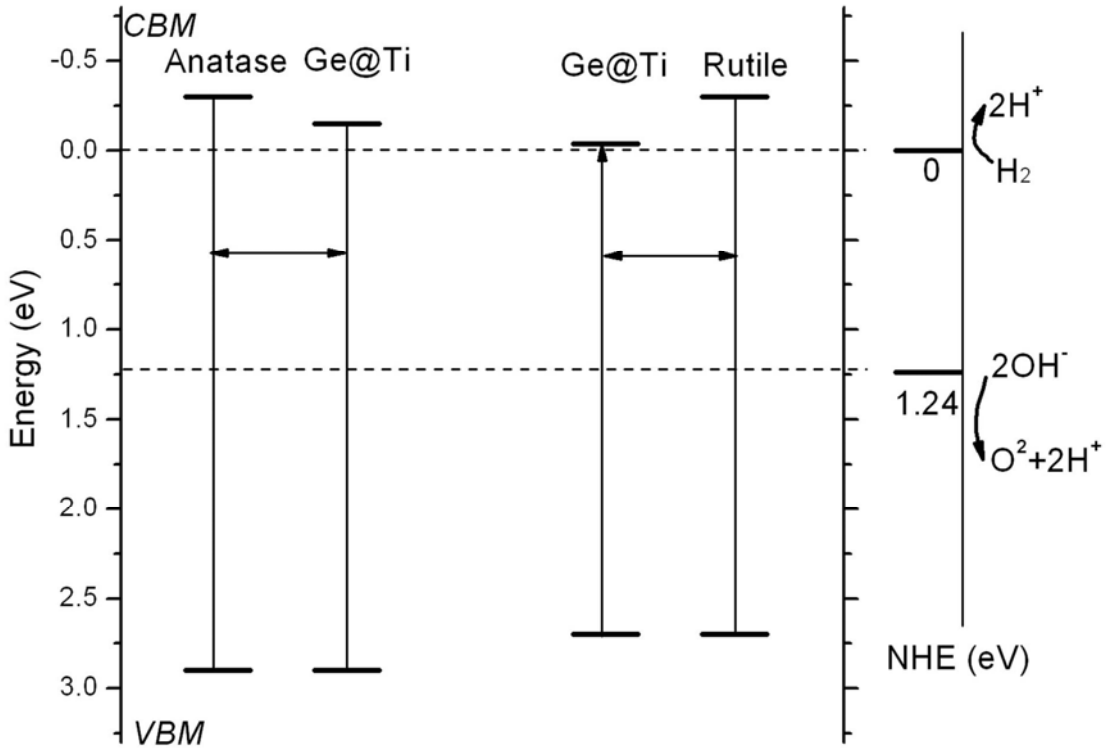
CBM
Anatase
Ge@Ti
Ge@Ti
Rutile
-0.5
0.0
0.5
1.0
1.5
2.0
2.5
3.0
Energy (eV)
VBM
2H+
H2
0
2OH-
1.24
O2+2H+
NHE (eV)

Figure 7

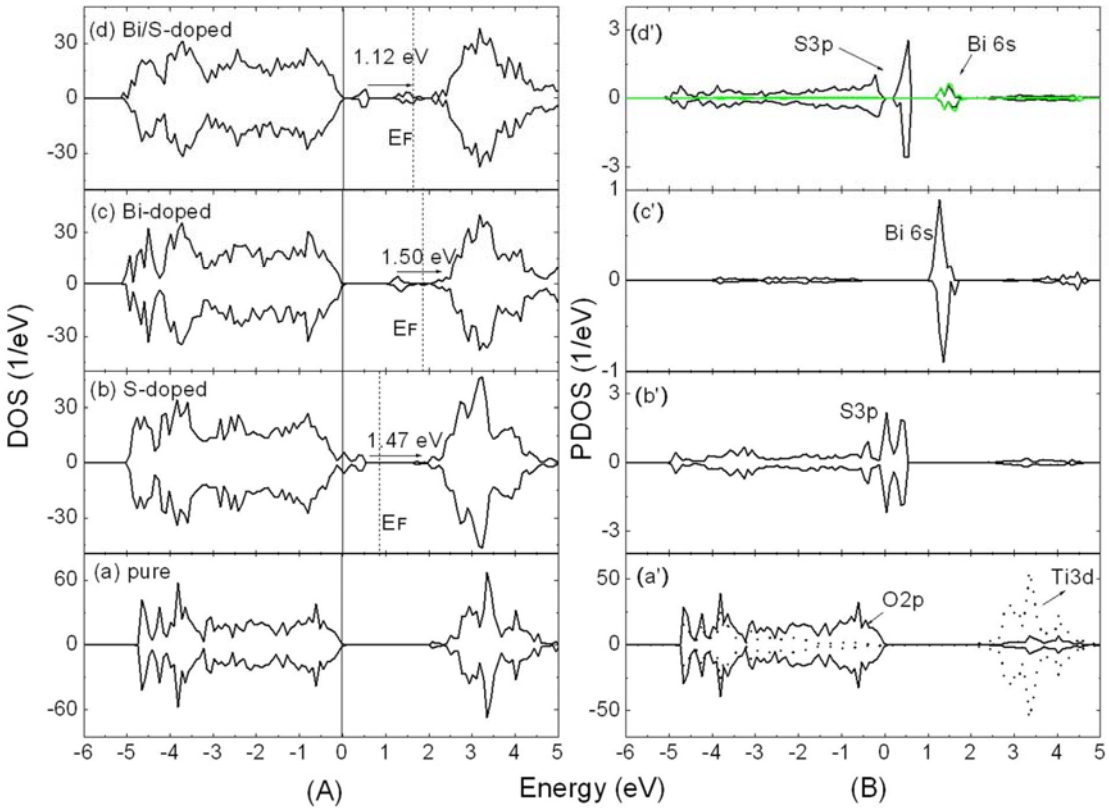
(d) Bi/S-doped
1.12 eV
EF
(c) Bi-doped
1.50 eV
EF
(b) S-doped
1.47 eV
EF
(a) pure
DOS (1/eV)
(A)
(d')
S3p
Bi 6s
(c')
Bi 6s
(b')
S3p
(a')
O2p
Ti3d
PDOS (1/eV)
Energy (eV)
(B)

Figure 8

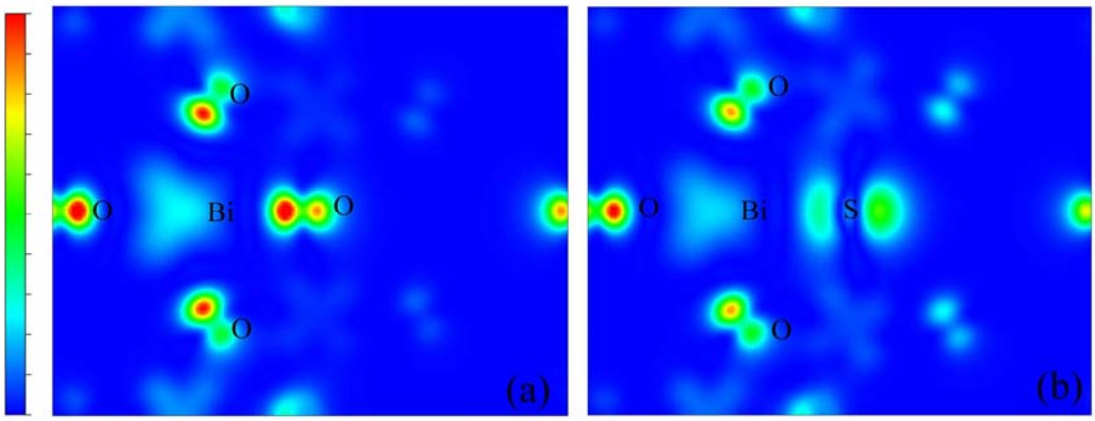

Figure 9

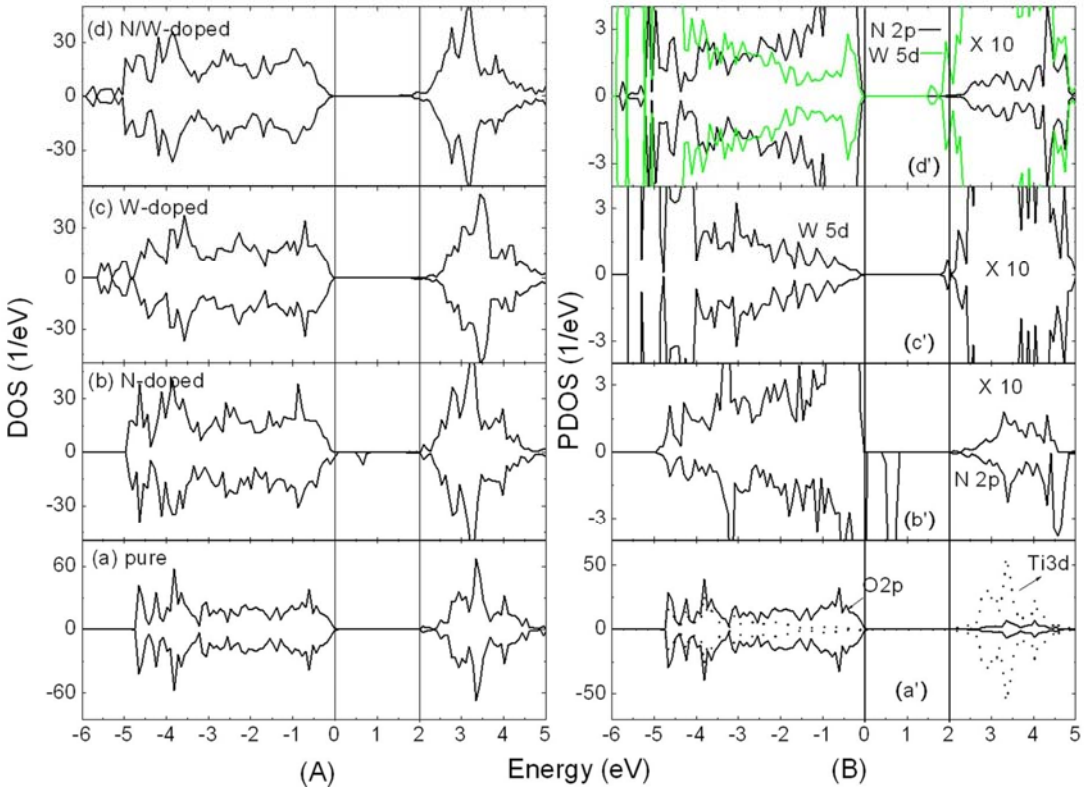
(d) N/W-doped
(c) W-doped
(b) N-doped
(a) pure
DOS (1/eV)
PDOS (1/eV)
N 2p
W 5d
X 10
(d')
W 5d
X 10
(c')
X 10
N 2p
(b')
O2p
Ti3d
(a')
(A)
Energy (eV)
(B)

Figure 10

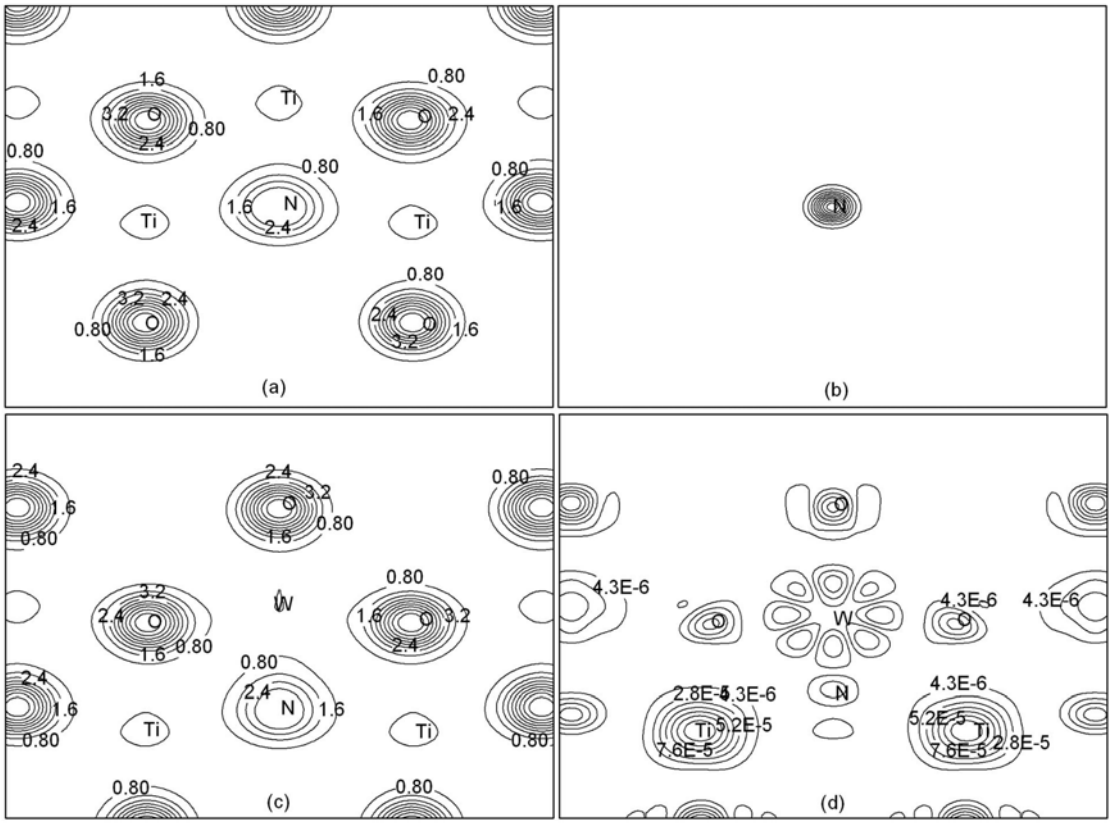

Figure 11